Atomistic simulation model on a diffusive timescale based on the extension of the cluster-activation method to continuous space

Ryo Yamada* and Munekazu Ohno
Division of Materials Science and Engineering, Faculty of Engineering, Hokkaido University, Kita 13 Nishi 8, Kita-ku, Sapporo, Hokkaido 060-8628, Japan

(Received 1 August 2022; accepted 11 April 2023; published 27 April 2023)

Recently the phase-field crystal method has attracted considerable attention because it can simulate the atomic behavior of a system on a diffusive timescale. In this study an atomistic simulation model is proposed, which is an extension of the cluster-activation method (CAM) from discrete to continuous space. This approach, called the continuous CAM, can simulate various physical phenomena of atomistic systems on diffusive timescales and employs well-defined atomistic properties, such as interatomic interaction energies, as the main input parameters. The versatility of the continuous CAM was investigated by performing simulations of crystal growth in an undercooled melt, homogeneous nucleation during solidification, and formation of grain boundaries in pure metal.

DOI: 10.1103/PhysRevE.107.045307

I. INTRODUCTION

Molecular dynamics (MD) and kinetic Monte Carlo (kMC) methods have been used to investigate the atomistic behavior of materials. The rapid increase in computational power and the development of efficient numerical schemes have gradually increased the range of applications for these approaches; however, their applicability is limited to extremely small time and space scales. For instance, it is challenging to deal with the time evolution of atomistic states on a diffusive timescale using MD simulation. Although kMC can be applied to diffusive timescales, accurate determination of the statistical nature of dynamics, for instance, in multicomponent alloys, entails massive computational work. Continuum models, such as the phase-field method (PFM), have been broadly employed to describe the microstructural phenomenon. However, the atomic information is not explicitly considered, and the phenomenological nature of such models inevitably restricts their ability to discover unexpected dynamics and/or mechanisms behind the phenomena of interest. Therefore, it is important to develop an approach for describing the evolution of the atomistic states on a diffusive timescale.

The use of MD and kMC models for atomistic simulations generally includes "nonproductive" back-and-forth atomic movements, such as atomic vibrations, where "productive" movements are rare events. This is the main reason why these methods cannot simulate phenomena on a diffusive timescale: the "nonproductive" events result in a waste of computational resources [1]. Unlike the MD and kMC models, there are several methods that capture only "productive" events, such as the phase-field crystal (PFC) method [2,3] and atomic density functional theory (ADFT) [1]. The PFC method and ADFT have attracted considerable attention because they can simulate atomistic behaviors on a diffusive timescale. In particular, the PFC method is versatile and has been used to simulate a variety of phenomena, such as solidification, nucleation, phase separation, and dislocation dynamics [2–8]. Quantitative PFC modeling has been conducted by linking it with the classical density functional theory of freezing using certain approximations [9–11]. The PFC models developed in the early works are the one-mode models, in which the dynamics are disregarded except near the first critical peak of density waves [10,12]. The accuracy can be improved using two-mode [11,13] and multimode [14] PFC models, but since these models require high computational costs, they have been employed in very few studies [15].

The cluster-activation method (CAM) is an atomistic simulation based on a microscopic master equation and concerns itself with diffusive time phenomena on an atomistic space scale [16]. Phase separation and/or ordering phenomena in alloys have been successfully described using the CAM [16–19]. In addition, the CAM has a significant advantage over PFC methods, as its input parameters are atomic interaction energy, attempt frequency, and activation energy for atomic jumps. The physical meanings of these terms are clear and, in principle, can be determined using other computational approaches, such as density functional theory (DFT) and MD simulations. However, the theoretical framework of CAM is entirely based on a rigid lattice system, and it cannot describe atomic displacement from Bravais lattice points. Therefore, the CAM cannot describe phase transitions that involve a change of Bravais lattice symmetry, such as face-centered cubic (fcc) to body-centered cubic (bcc) transitions, solidification, and the grain growth and formation of lattice defects in crystals. This study aims to address this limitation by extending the CAM to a continuous space.

The cluster variation method (CVM) [20] is one of the most reliable methods for calculating the configurational entropy of the metallic alloy systems. Although the original framework

*Corresponding author: ryamada@eng.hokudai.ac.jp

of the CVM is based on a rigid lattice (or Bravais lattice) as in the CAM, atomic displacements have been incorporated into the CVM by introducing quasilattice points around each Bravais lattice points; such a model is called the continuous-displacement CVM (CDCVM) [21]. In this study, the CAM is extended to a continuous space by employing an idea similar to that used in the CDCVM. This model, called the continuous CAM, enables atomistic simulations on a diffusive timescale from the input parameters of well-defined atomistic properties. This paper is organized as follows: First, the essential points of the CAM and its extension to a continuous space are described in Sec. II. A phase diagram and the microstructural evolution during solidification are calculated using the continuous CAM, and these results are compared with those using the PFC method, in Sec. III. Additionally, several applications of the continuous CAM are demonstrated, such as solidification, nucleation-growth behaviors, and grain boundary energies at various misorientations in pure metal. Finally, the results and methodology developed here are summarized in Sec. IV.

II. METHOD

Let us consider a multicomponent alloy consisting of m species (including the vacancies) in a crystal with a total number of sizes, N. For the original CAM, a rigid lattice is assumed. The spatial distribution of species i can be described by the single-site occupation probability $P_i(\mathbf{r})$, where $\mathbf{r}$ is the position of a lattice point. This satisfies the normalization condition given by $\sum_i^m P_i(\mathbf{r}) = 1$. When the vacancy-mediated mechanism is considered, the time evolution of $P_i(\mathbf{r})$ is described by the mean-field kinetic equation [17,22]:

$$\frac{dP_i(\mathbf{r})}{dt} = \sum_{\boldsymbol{\delta}} \sum_{\{X\}} P_{vi\{X\}}(\mathbf{r}+\boldsymbol{\delta},\ \mathbf{r}, \{\boldsymbol{x}\}) R_{vi}(\{X\}) - \sum_{\boldsymbol{\delta}} \sum_{\{X\}} P_{iv\{X\}}(\mathbf{r},\ \mathbf{r}+\boldsymbol{\delta}, \{\boldsymbol{x}\}) R_{iv}(\{X\}), \quad (1)$$

where t is the time, and v in the subscript represents the vacancy, the position of which is represented by $\mathbf{r}+\boldsymbol{\delta}$. $P_{ij\{X\}}(\mathbf{r},\ \mathbf{r}', \{\boldsymbol{x}\})$ is the joint probability of finding species i at $\mathbf{r}$, species j at $\mathbf{r}'$ and a set of atomic configurations $\{X\}$ at the other sites $\{\boldsymbol{x}\}$. $R_{ij}(\{X\})$ is the rate at which i and j species interchange their positions under the influence of $\{X\}$ and can be approximated using [16]

$$R_{ij}(\{X\}) = \nu \exp\left(-\frac{U_0}{k_B T}\right) \exp\left(-\frac{\Delta E(ij, \{X\})}{k_B T}\right), \quad (2)$$

where ν is the attempt frequency, U_0 is the activation energy, k_B is the Boltzmann constant, T is the temperature, and $\Delta E(ij, \{X\})$ is the change in energy when i and j species interchange their positions for a given $\{X\}$. The calculation of the time evolution of $P_i(\mathbf{r})$ requires the N-site occupation probability, $P_{vi\{X\}}(\mathbf{r},\ \mathbf{r}+\boldsymbol{\delta}, \{\boldsymbol{x}\})$, and it must be approximated using the occupation probabilities of smaller sites, that is, small clusters to make the calculation feasible. The maximum size of the cluster considered in the calculation determines the level of approximation of this method in a manner similar to that of the CVM. In general, it is reasonable to restrict $\boldsymbol{\delta}$ to the nearest-neighbor sites of $\mathbf{r}$ [17]. In addition, when

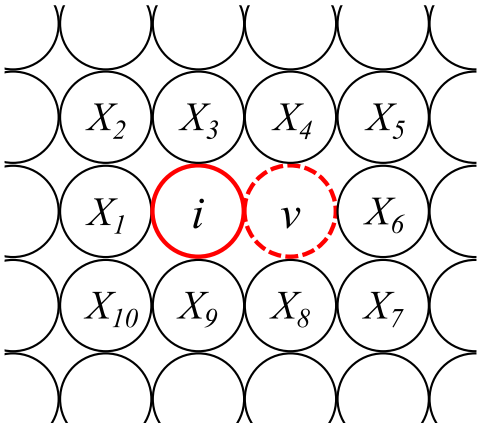

FIG. 1. Schematic depicting an i-v pair cluster, where the first and second nearest-neighboring atoms are numbered from 1 to 10 [16].

$\{\boldsymbol{x}\}$ is limited to the nearest-neighbor sites of $\mathbf{r}$ and $\mathbf{r}+\boldsymbol{\delta}$, as shown in Fig. 1, the time evolution of the cluster probability of the nearest-neighbor pair is coupled to Eq. (1) using the superposition approximation of the cluster probability of triplet clusters, as detailed by Geng and Chen [17]. This corresponds to the pair approximation. The simplest approximation for $P_{ij\{X\}}(\mathbf{r},\ \mathbf{r}+\delta, \{\boldsymbol{x}\})$ is given by [16]

$$P_{ij\{X\}}(\mathbf{r},\ \mathbf{r}+\delta, \boldsymbol{x}) = P_i(\mathbf{r}) P_j(\mathbf{r}+\delta) P_{X_1}(\boldsymbol{x}_1) P_{X_2}(\boldsymbol{x}_2) \cdots P_{X_n}(\boldsymbol{x}_n), \quad (3)$$

which corresponds to the point approximation in the CVM. Note that Eq. (1) is completely based on the atomistic master equation, and it does not rely on the free energy.

In the conventional CAM described above, a rigid lattice (Bravais lattice) is assumed. Quasilattice points are introduced around each Bravais lattice point to describe the atomic displacement in the CDCVM. The Bravais lattice is not considered for continuous CAM developed in this study; instead, a system composed only of quasilattice points is considered (see Fig. 2). The main difference between the conventional and continuous CAMs is that the nearest-neighbor sites $\boldsymbol{\delta}$ in Eq. (1) become quasilattice sites instead of Bravais lattice sites in continuous CAM. This allows the liquid phase to be characterized by the uniform distribution of $P_i(\mathbf{r})$, where $\mathbf{r}$ indicates the quasilattice sites, and the crystalline materials to be described by the spatial distribution of $P_i(\mathbf{r})$, with peaks according to the symmetry of the crystal. The atomic configuration is fully described by the spatial distribution of $P_i(\mathbf{r})$ in an approach similar to that of the PFC method. Therefore, this strategy can deal with a wide range of phase transition phenomena, including the formation of lattice defects, such as dislocations and grain boundaries.

In this study, we employed the point approximation given in Eq. (3). Furthermore, although ν and U_0 are, in principle, dependent on the type of i-j pair and the atomic configurations of its surroundings, they are assumed to be constant in accordance with the early work [17]. Importantly, it remains unclear if an exponential term is required in the theoretical framework with the quasilattice. The point will be investigated in a future work. In this study, timescale is normalized by

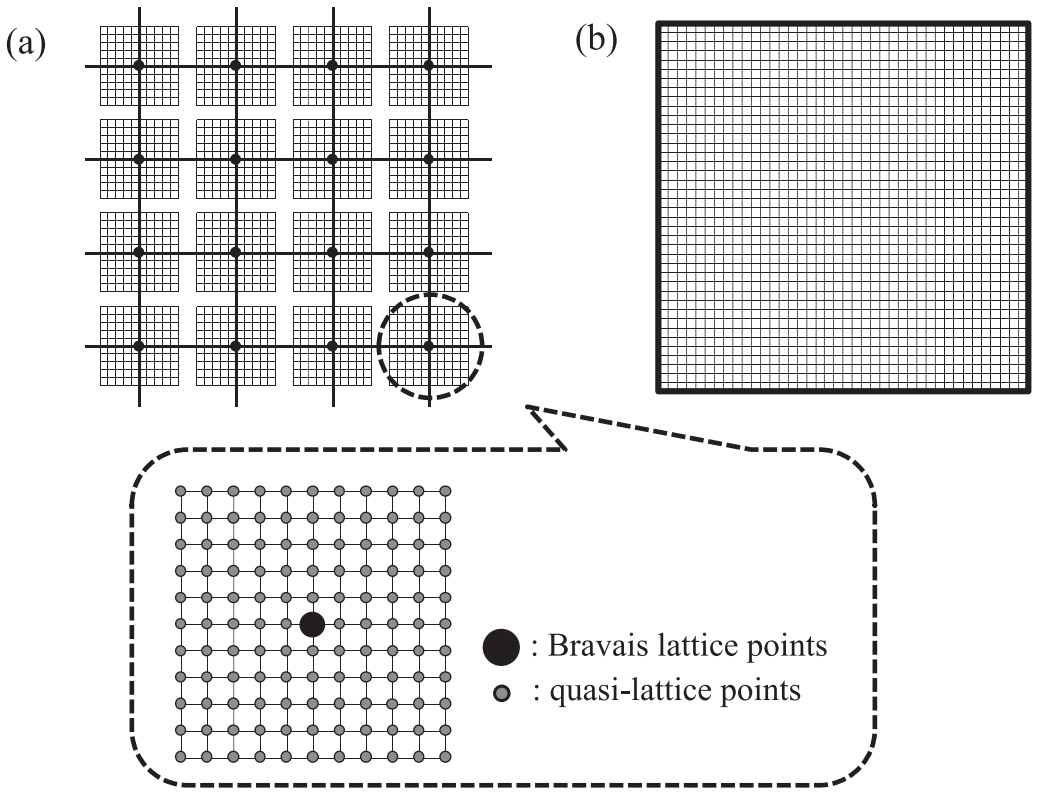

FIG. 2. Lattice systems for the (a) CDCVM and (b) continuous CAM. The system in the CDCVM is composed of Bravais lattice points, each of which is surrounded by quasilattice points, whereas the system in the continuous CAM is composed of only quasilattice points.

$\nu' \equiv \nu \exp(-\frac{U_0}{k_B T})$ for the sake of simplicity. In this case, the atomic interaction energy in Eq. (2) is the only input parameter, and although a reliable atomic potential energy, such as the embedded atom method (EAM), can be used, the following Lennard-Jones potential is utilized in this work for simplicity:

$$e_{ij} = e^0_{ij}\left[\left(\frac{r^0_{ij}}{r_{ij}}\right)^{12} - 2\left(\frac{r^0_{ij}}{r_{ij}}\right)^{6}\right], \tag{4}$$

where e_{ij} and r_{ij} are the pair interaction energy and interatomic distance between i and j atoms, respectively, and e^0_{ij} and r^0_{ij} are those at the minimum pair interaction energy. Here a model system is considered using the normalization of e_{ij} and r_{ij} by e^0_{ij} and r^0_{ij}, respectively.

In addition, a two-dimensional simulation system is adopted. A first-order Euler scheme is employed to solve Eq. (1), and a periodic boundary condition is applied. The energy cutoff radius is set to $r_{\text{cutoff}}/r^0_{ij} \approx 1.414$, and the following grid size is used: $dx/r^0_{ij} = dy/r^0_{ij} = 0.1$. The simulation does not work well for small interatomic distances, because the exponential term in Eq. (2) becomes infinite, which is ascribed to the self-interaction energy. To avoid this issue, the screening energy is defined as $e_{\text{screening}}/e^0_{ij} = 10.0$. When the interatomic energy is higher than $e_{\text{screening}}$, it is treated as $e_{ij} = e_{\text{screening}}$.

Although this is the simplest approximation, Eq. (3) is acceptable for the continuous CAM and is used in the present study. Within the theoretical framework of conventional CAM, it is well known that short-range correlations play an important role in alloy systems [16], and information on larger clusters compared to point clusters (or atomic concentrations) is necessary to reliably estimate phase equilibria [23]. However, the effect of short-range correlations becomes insignificant in the continuous CAM because most sites are not occupied by atoms (as seen in the following results), which is compatible with the calculations for dilute alloy systems in the conventional CAM where configurational entropy can be adequately estimated using only the point cluster probability.

III. RESULTS AND DISCUSSION

A. Equilibrium states

First, the solidus line between liquid and solid (or triangular phase) in pure metal A is determined by identifying the final microstructure for a given set of initial atomic densities, or probabilities, P^0_A, and temperatures, $k_B T/e^0_{AA}$. To determine the solidus line, a small system (the grid number: 200×200) was used. It was found that the triangular phase is a stable structure when the atomic density P^0_A is relatively small: $P^0_A \approx 0.01$. The physical interpretation of the atomic density is that there are, for example, one, two, and three A-type atoms in 10×10 grids for $P^0_A = 1.0$, 2.0, and 3.0, respectively. To avoid forming a metastable configuration, such as a square lattice, a small amount of noise was incorporated throughout the entire system during the time evolution process, where the nucleus of a triangular phase was placed in the initial state at the center of the system.

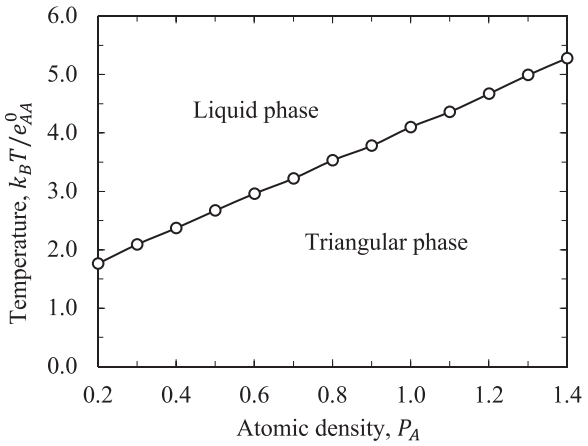

FIG. 3. Calculated solidus line between the liquid and triangular phases using the continuous CAM, where $e_{\text{screening}}/e^0_{AA}$ is set to 10.0.

Figure 3 shows that the solidus line, or melting temperature, linearly increases with atomic density, which is consistent with the phase diagram determined from the experiments and MC simulations [24], as well as the PFC method [3]. It was not easy to identify a liquidus line using the present approach, and it is not shown here. To determine a liquidus line, an approach based on free energy should be required, as is done in the PFC method [3], but it is beyond the scope of the present work.

It was found that the phase boundary depends on $e_{\text{screening}}$; a smaller $e_{\text{screening}}$ results in a solidus line that lies in the lower temperature region. This dependency can be avoided by using the different pair interaction energies, such as those proposed by Jin and Khachaturyan [1] (see Appendix A 1). In this study, Eq. (4) with $e_{\text{screening}}$ is used throughout the following calculations in Secs. III B and III A.

B. Comparison with the PFC method

Next, the two-dimensional solidified microstructures calculated using the continuous CAM are compared with those obtained using the PFC method. The calculated microstructures of the continuous CAM for pure metal A at $k_BT/e^0_{AA} = 3.0$ are shown in Fig. 4. Here various initial atomic densities, $P^0_A = 1.0$, 2.0, and 3.0, were assumed, and a small amount of noise was introduced at the center of the system in the initial states. As seen in the figure, the system takes various states by changing P^0_A: the triangular phase, coexisting phases of triangular and stripe phases, and strip phase. These results correspond to those obtained using the PFC method.

The solidified microstructures calculated using the PFC method for $\phi_0 = -0.30$, -0.15, and -0.05 at $\varepsilon = -0.5$, where ϕ_0 represents the initial density of the system and ε corresponds to the supercooling temperature, are shown in Fig. 5 (see the Appendix A 2 for the calculation details). A small amount of noise was introduced in the initial states, as was done in the microstructure in Fig. 4. The atomic densities at each site are plotted in the figure, where each panel represents the triangular phase, coexisting phases of triangular and stripe phases, and stripe phase, respectively, all of which correspond to the expected atomic configurations from the calculated phase diagram (Fig. 5 in Ref. [3]).

Although there is a slight difference between the solidified microstructures obtained using the continuous CAM and those using the PFC method, the same atomic configurations are produced, such as the triangular phase, stripe phase, and their coexisting phases. This result suggests that a phase diagram similar to that obtained from the PFC method exists in the case of the continuous CAM. Notably, the results show that the continuous CAM can simulate a solidification process using only the pair interaction energy except for the time-related parameters, such as the attempt frequency and activation energy.

C. Applications of the continuous CAM

The analysis of solidification, nucleation and growth, and grain boundary energy at various misorientation angles in pure metal A are explored here to understand the versatility of the continuous CAM. The initial atomic density was set to $P^0_A = 1.0$ in all calculations shown here.

The calculated growth process of a solid nucleus in the liquid phase is shown in Fig. 6, where the nucleus of the triangular phase is placed at the center of the system in the initial state. The temperature was set to $k_BT/e^0_{AA} = 4.0$ ($T/T_m = 0.976$), and the grids number used is 3000×3000. An anisotropic morphology is observed in the solidified microstructure, and a similar morphology has been produced in pure metal using the PFM (see Ref. [25]). Note that the equilibrium symmetry of a triangular lattice should be sixfold

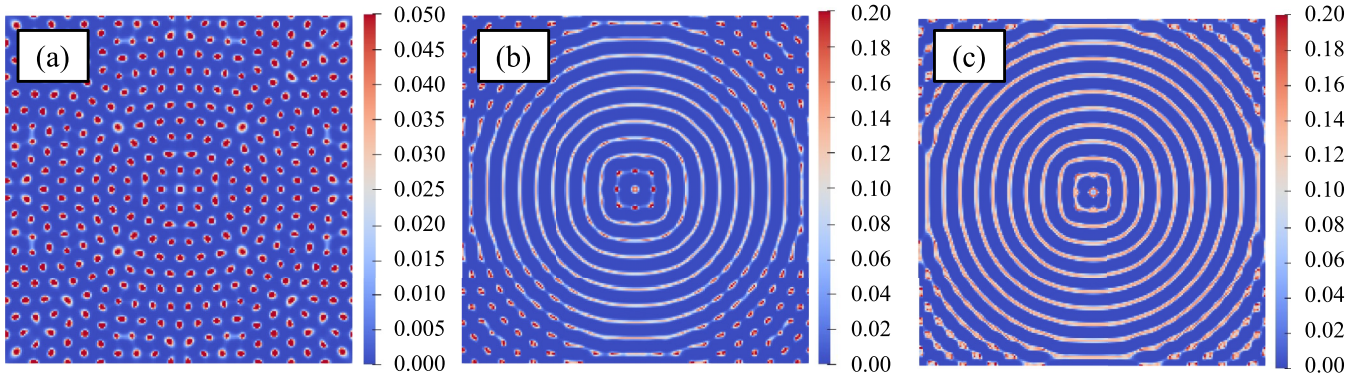

FIG. 4. Calculated two-dimensional solidified microstructures using the continuous CAM for $P^0_A = 1.0$, 2.0, and 3.0 at $k_BT/e^0_{AA} = 3.0$. The color bar represents the local atomic density, P^0_A. Here 200×200 grids are used for the calculations.

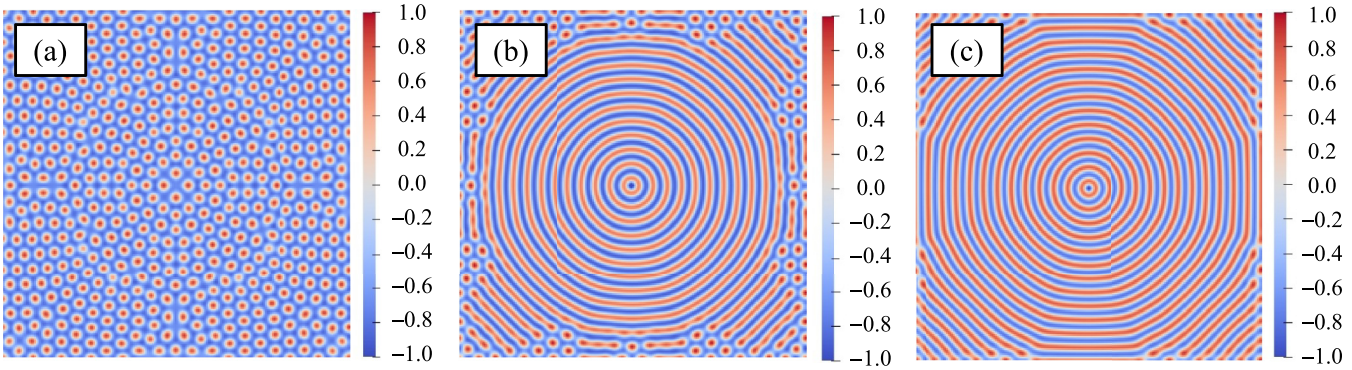

FIG. 5. Calculated two-dimensional solidified microstructures using the PFC method for $\phi_0 = -0.30$, -0.15, and -0.05 at $\varepsilon = -0.5$ [28]. The color bar represents the phase-field parameter ϕ. Here 200×200 grids are used for the calculations.

in a "single" crystal, but the one obtained here is fourfold. This is due to the formation of nucleus next to the initial nucleus as seen in Fig. 6(c). Thus, the calculated solid microstructure includes grain boundaries as well as dislocations. It is expected that a sixfold symmetry can be obtained by adjusting atomic density and degree of undercooling. It is also noteworthy that it was confirmed that the solidified morphology is rotated with the rotation of the initial nucleus. This suggests that the fourfold symmetry is inherent of the system, not caused by the computational procedure employed here (i.e., finite difference calculation).

Although a solid nucleus was placed in the initial state in the previous application (Fig. 6), it can spontaneously form, i.e., homogeneous nucleation, within the theoretical framework of the continuous CAM. The solidification process from a liquid phase is shown in Fig. 7, where a small amount of noise is introduced throughout the system, and the temperature is set to $k_B T/e^0_{AA} = 4.0$ $(T/T_m = 0.976)$. First, a squarelike configuration is formed from the liquid phase, and subsequently, triangular phases are nucleated. Grain coarsening of the triangular phase then can be observed. It is considered that a squarelike configuration is formed before

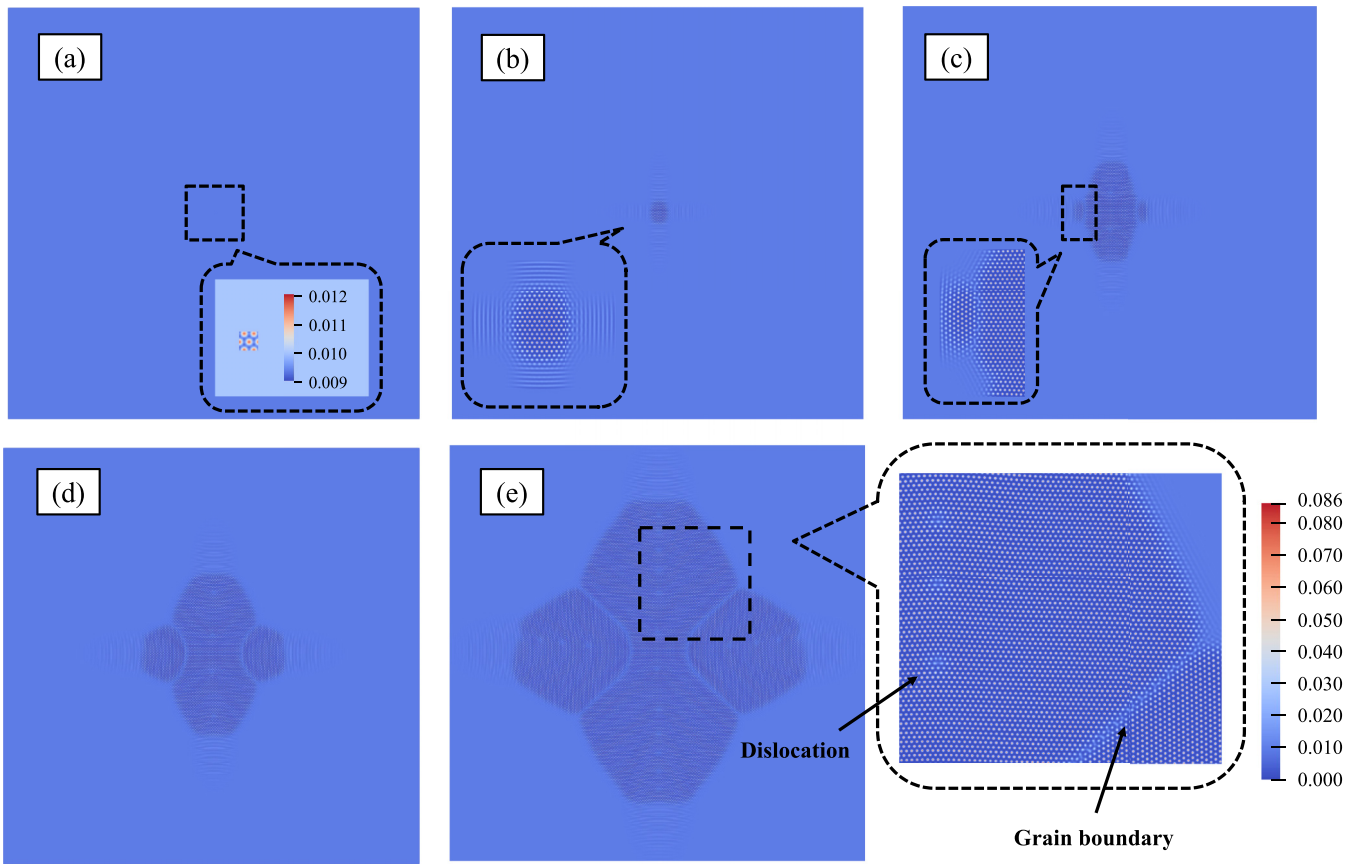

FIG. 6. Calculated two-dimensional solidified microstructure in pure metal using the continuous CAM at (a) $t' = 0.0$, (b) $t' = 20.0$, (c) $t' = 30.0$, (d) $t' = 40.0$, and (e) $t' = 60.0$, where a nucleus of triangular phase nucleus is placed at the center of the system in the initial state.

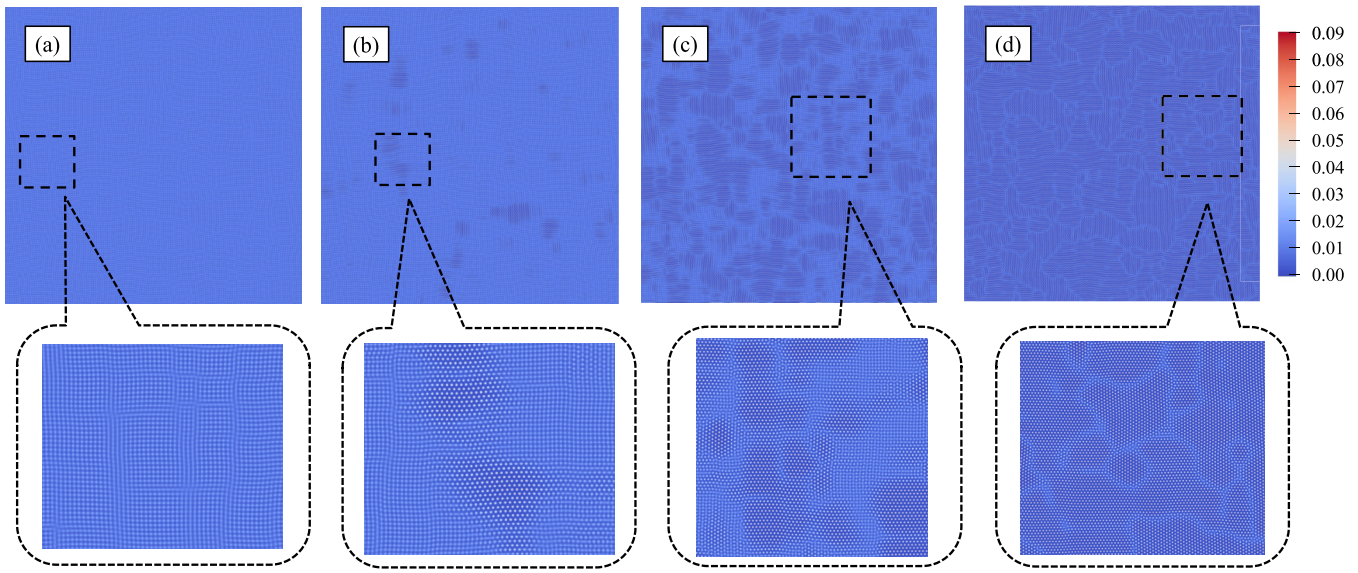

FIG. 7. Temporal change of solidified microstructures in pure metal at (a) $t' = 30.0$, (b) $t' = 33.0$, (c) $t' = 35.0$, and (d) $t' = 37.0$, where a small amount of noise is incorporated throughout the system. Here 3000 × 3000 grids are used for the calculation.

a stable triangular phase, because of its low density compared with that of the triangular phase. This precursor phenomenon, i.e., the formation of a squarelike configuration before the triangular phase, is similar to the appearance of a bcc-like configuration before a stable fcc phase from an undercooled melt [26].

Finally, grain boundary configurations and their energies at various misorientation angles were calculated, as shown in Fig. 8. Here a rectangular system with 1000 × 4000 grid points was used, and two solids with different crystal orientations were aligned along the y axis with a liquid phase filled between them. By running simulations at $k_BT/e^0_{AA} = 3.5$ ($T/T_m = 0.854$), the grain boundaries with various misorientation angles were formed (see Fig. 9). The grain boundary energy was determined by comparing the free energy of the systems with and without grain boundaries. The free energy, F, of a system is computed as follows:

$$F = \frac{1}{2}\sum_{\mathbf{r},\,\mathbf{r}'}\sum_{i,j} e_{ij}(\mathbf{r}-\mathbf{r}')P_i(\mathbf{r})P_j(\mathbf{r}') + k_BT\sum_{\mathbf{r}}\sum_{i} P_i(\mathbf{r})\ln P_i(\mathbf{r})\,. \tag{5}$$

To remove strain effects, the area without the edge of the system was considered here: the area from $N_y/5$ to $4 \times N_y/5$, where N_y is the number of grid points along the y axis. As can be seen in Fig. 8, the grain boundary energy monotonically increases with the misorientation angle, and different increasing tendencies can be observed for small and large misorientation angles (below and above 15°). This difference originates from the grain boundary changing from coherent to

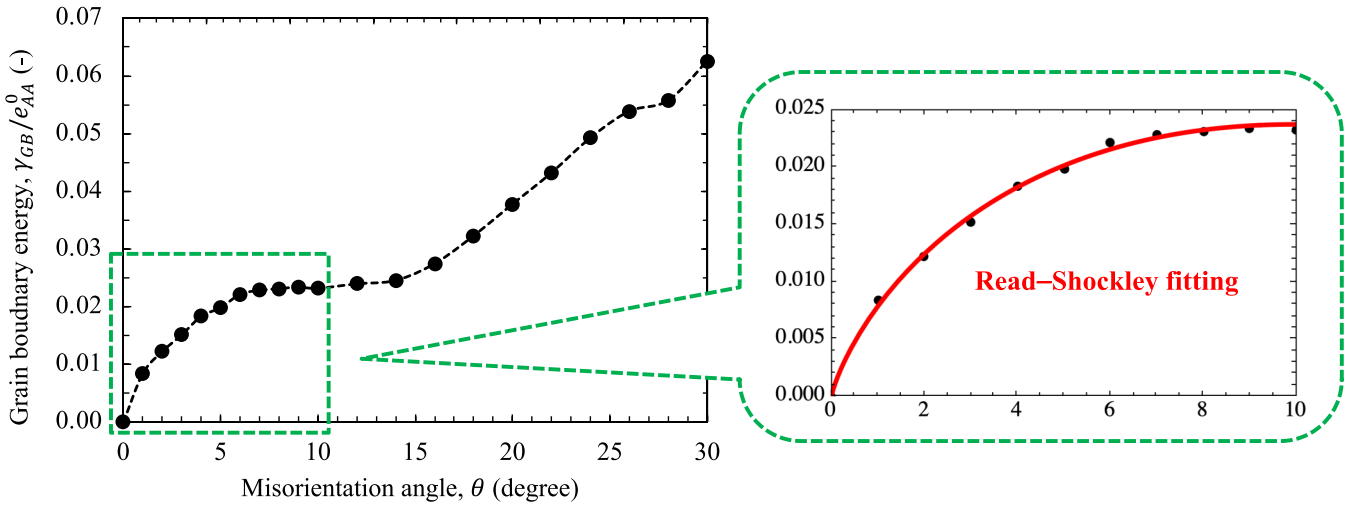

FIG. 8. Grain boundary energies at various misorientation angles. The energies at small misorientation angles are fitted to the Read-Shockley relation ($\gamma^0_{GB} = 3.30$ and $C = 0.00239$).

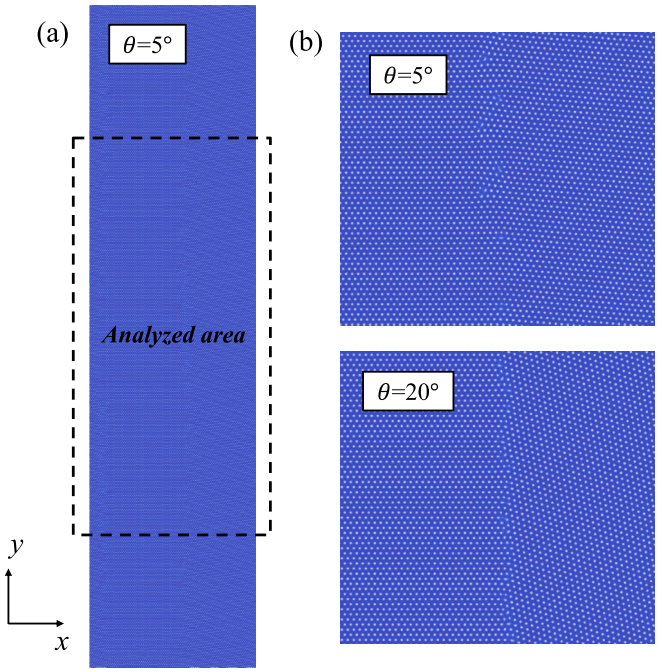

FIG. 9. Simulated grain boundaries (a) the whole system at $\theta = 5^\circ$ and (b) the magnified ones at $\theta = 5^\circ$ and 20°. Here the area used for the calculation of the grain boundary is represented by the broken line.

incoherent at around 15° (see Fig. 9). Furthermore, the grain boundary energies at low misorientation angles (less than 10°) were fitted to the following Read-Shockley relation [27]:

$$\gamma_{GB} = \gamma^0_{GB}\theta(C - \ln\theta), \tag{6}$$

where γ^0_{GB} and C are constants. From the figure, it can be observed that the calculated grain boundary energies follow the Read-Shockley relation at low misorientation angles. This suggests that the continuous CAM developed in this study is reliable.

IV. CONCLUSION

The continuous CAM was developed by incorporating the idea of the CDCVM into the conventional CAM: i.e., the incorporation of quasilattice points into a system. The calculated solidified microstructures of pure metal were compared with those obtained using the PFC method, and it was found that similar atomic configurations were obtained. Furthermore, the continuous CAM was demonstrated in several applications, including the analysis of solidification, nucleation-growth processes, and grain boundary energies at various misorientation angles in pure metal. Interesting behavior was observed for each application. In the solidification process, the anisotropic morphology of the solid phase was generated naturally, and it was found that a solidified crystal contains grain boundaries and dislocations. In the nucleation-growth process, a square lattice was formed just before a stable triangular lattice was nucleated. The nuclei of the triangular lattice grew and developed grain boundaries; subsequently, grain-coarsening behavior was observed. In the calculation of grain boundary energies, it was found that the energy monotonically increased with the misorientation angles. The rate of increase changed between coherent and incoherent grain boundaries, and the grain boundary energies followed the Read-Shockley relation at low misorientation angles.

Note that the continuous CAM developed in this study uses well-defined atomistic properties, such as interatomic interaction energies, as its main input parameters. Furthermore, the theoretical framework does not rely on free energy, indicating that it has the potential to explore the dynamics of various phenomena far from the equilibrium states. It is also noteworthy that although time was normalized in the present calculations, a real-time scale can be incorporated as in the kMC simulations when the attempt frequency and activation energy for an atomic jump are given.

It is noteworthy, however, that the liquidus line calculated using MC simulations is not quantitatively reproduced when the potential form of Eq. (A1) was used within the present model, as seen in Fig. 11 in the Appendix. Searching for an appropriate form of potential suited for the present model is an important issue and remains as a future work.

The data supporting the findings of this study are available from the corresponding author upon reasonable request.

ACKNOWLEDGMENTS

This work was supported by a KAKENHI, Grant-in-Aid for Young Scientists (No. 22K14462) from the Japan Society for the Promotion of Science (JSPS).

APPENDIX

1. Revised pair interaction energy

The deficiency of the pair interaction energy discussed in Sec. III A may be avoided using the following pair interaction

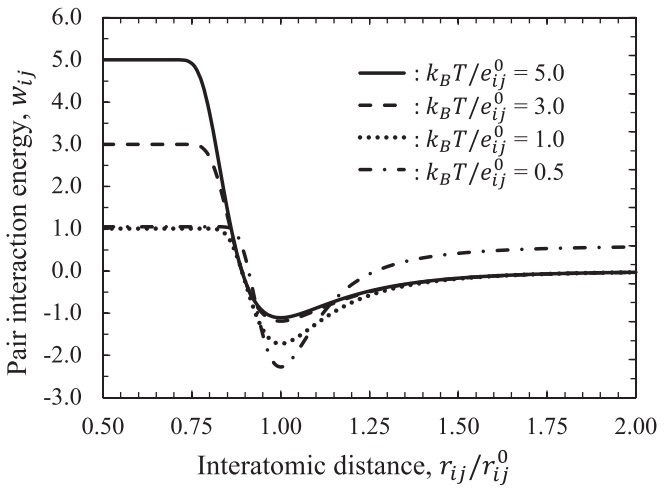

FIG. 10. Graph of the pair interaction energy, w_{ij}, shown in Eq. (A1) at different interatomic distances, where the Lennard-Jones potential [Eq. (4)] is used for e_{ij}.

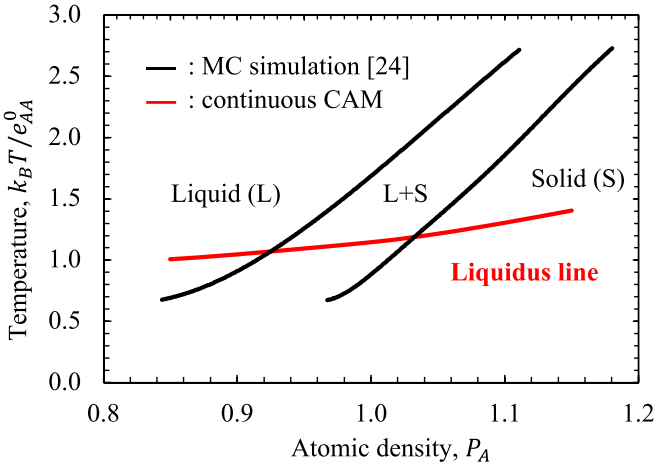

FIG. 11. Calculated liquidus line between the liquid and triangular phases in three dimensions using the continuous CAM, where Eq. (A1) is used for the pair interaction energy. Here the liquidus and solidus lines determined from MC simulations are shown together [24].

energy, w_{ij}, proposed by Jin and Khachaturyan [1]:

$$w_{ij} = k_BT\left[1 - \exp\left(-\frac{e_{ij}}{k_BT}\right)\right]. \quad \text{(A1)}$$

This potential energy equation substituted with Eq. (4) yields a constant energy for a small interatomic distance, as was assumed in the presented calculations (see Fig. 10). The liquidus line between the liquid and triangular phases was calculated using Eq. (A1) in three dimensions, and it is shown in Fig. 11, where the liquidus and solidus lines determined by MC simulations are shown together [24]. The liquidus line increases with atomic density, which is consistent with the result of MC simulation. However, there is some discrepancy in the calculated liquidus lines using the present model and MC simulations. The main reason for this discrepancy is due to the use of Eq. (A1). Although there is no need to set a screening energy in this potential and the estimated liquidus line is uniquely determined, the physical origin of this potential is still unclear. It is expected that an appropriate form of potential will improve the calculated results.

2. PFC method

The PFC method originates from the PFM and uses a phase-field parameter to describe the atomic configuration. In the simplest approximation, the free energy of a system is given by [2,3]

$$\tilde{F} = \int_V \left\{\frac{\tilde{\phi}}{2}\left[\alpha\Delta T + \lambda\left(q_0^2 + \nabla^2\right)^2\right]\tilde{\phi} + \frac{1}{4}u\tilde{\phi}^4\right\}dV, \quad \text{(A2)}$$

where $\tilde{\phi}$ is the phase-field parameter, V is the volume, q_0 is the wave number, ΔT is the supercooling temperature, and α, λ, and u are material-specific constants. Equation (A2) is normalized as [2,3]

$$F = \int_V \left[\frac{1}{2}(\varepsilon+1)\phi^2 + \frac{1}{4}\phi^4 + \phi\nabla^2\phi + \frac{1}{2}\phi\nabla^4\phi\right]dV, \quad \text{(A3)}$$

where $F \equiv u\tilde{F}/\lambda^2 q_0^5$, $x \equiv \tilde{x}q_0$, $\phi \equiv \tilde{\phi}\sqrt{u/\lambda q_0^4}$, and $\varepsilon \equiv \alpha\Delta T/\lambda q_0^4$. Following the Cahn-Hilliard equation, the time evolution of ϕ is given by [2,3]

$$\frac{\partial\phi}{\partial t} = \nabla^2\left\{[\varepsilon + (1+\nabla^2)^2]\phi + \phi^3\right\}. \quad \text{(A4)}$$

In order to solve Eq. (A4), a first-order Euler scheme was used for the time derivative, and the spherical Laplacian approximation was used to compute all Laplacians [3].

[1] Y. M. Jin and A. G. Khachaturyan, J. Appl. Phys. **100**, 013519 (2006).
[2] K. R. Elder, M. Katakowski, M. Haataja, and M. Grant, Phys. Rev. Lett. **88**, 245701 (2002).
[3] K. R. Elder and M. Grant, Phys. Rev. E **70**, 051605 (2004).
[4] J. Berry, M. Grant, and K. R. Elder, Phys. Rev. E **73**, 031609 (2006).
[5] K. R. Elder, N. Provatas, J. Berry, P. Stefanovic, and M. Grant, Phys. Rev. B **75**, 064107 (2007).
[6] T. Hirouchi T. Takaki, and Y. Tomita, Comput. Mater. Sci. **44**, 1192 (2009).
[7] V. Fallah, N. Ofori-Opoku, J. Stolle, N. Provatas, and S. Esmaeili, Acta Mater. **61**, 3653 (2013).
[8] P. Jreidini, G. Kocher, and N. Provatas, Phys. Rev. E **97**, 042802 (2018).
[9] K.-A. Wu and A. Karma, Phys. Rev. B **76**, 184107 (2007).
[10] K.-A. Wu, A. Adland, and A. Karma, Phys. Rev. E **81**, 061601 (2010).
[11] E. Asadi and M. A. Zaeem, JOM **67**, 186 (2015).
[12] A. Jaatinen, C. V. Achim, K. R. Elder, and T. Ala-Nissila, Phy. Rev. E **80**, 031602 (2009).
[13] E. Asadi and M. A. Zaeem, Comput. Mater. Sci. **105**, 110 (2015).
[14] S. K. Mkhonta K. R. Elder, and Z.-F. Huang, Phys. Rev. Lett. **111**, 035501 (2013).
[15] A. Nourian-Avval and E. Asadi, Comput. Mater. Sci. **128**, 294 (2017).
[16] L.-Q. Chen and J. A. Simmons, Acta Metall. **42**, 2943 (1994).
[17] C. Geng and L.-Q. Chen, Scr. Metall. Mater. **31**, 1507 (1994).
[18] C. Geng and L.-Q. Chen, Surf. Sci. **355**, 229 (1996).
[19] L.-Q. Chen, Phys. Rev. B **58**, 5266 (1998).
[20] R. Kikuchi, Phys. Rev. **81**, 988 (1951).
[21] R. Kikuchi, J. Phase Equilibria **19**, 412 (1998).
[22] J.-F. Gouyet, M. Plapp, W. Dieterich, and P. Maass, Adv. Phys. **52**, 523 (2003).
[23] T. Mohri, JOM **65**, 1510 (2013).
[24] J.-P. Hansen and L. Verlet, Phys. Rev. **184**, 151 (1969).
[25] R. Kobayashi, Physica D **63**, 410 (1993).
[26] P. R. ten Wolde, M. J. Ruiz-Montero, and D. Frenkel, Phys. Rev. Lett. **75**, 2714 (1995).
[27] W. T. Read and W. Shockley, Phys. Rev. **78**, 275 (1950).
[28] T. Takaki and A. Yamanaka, Phase-field model (in Japanese), Yokendo, Tokyo, 2012.